Received: 29 November 2023 | Revised: 4 April 2025 | Accepted: 8 May 2025

DOI: 10.33012/navi.702

REGULAR PAPERS

Ranging Performance Evaluation for Higher-Order Scalable Interplex

Florian C. Beck*[1, 2] | **Christoph Enneking**[1] | **Steffen Thölert**[1,2] | **Felix Antreich**[3]

[1] Institute of Communications and Navigation German Aerospace Center (DLR), Wessling, Germany

[2] Chair of Navigation RWTH Aachen University, Aachen, Germany

[3] Department of Telecommunications, Aeronautics Institute of Technology (ITA), São José dos Campos, Brazil

Correspondence
Florian Beck
Münchener Str. 20
82234 Wessling, Germany
Email: florian.beck@dlr.de

Abstract

Scalable interplex represents a multiplexing technique that has been specifically designed to modify a signal constellation in order to adapt the transmitted signal to the characteristics of a high-power amplifier and thereby enhance the received power of the navigation signals. This paper builds upon existing knowledge regarding the trade-off between increased usable signal power and amplifier efficiency when scaling intermodulation (IM) terms, with a particular focus on the Galileo E1 signals and one potential additional signal candidate. The scalable interplex is optimized based on the achievable joint receiver efficiency. The aim of this study is to determine whether this signal constellation optimization also results in a reduction in code tracking jitter. The findings indicate that in numerous instances, the scalable interplex achieves a reduction in code tracking jitter by scaling specific IM terms in comparison with a constant-envelope six-channel interplex.

Keywords

efficiency, GNSS, multiplexing

1 | INTRODUCTION

Current global navigation satellite systems (GNSSs) provide positioning, navigation, and timing (PNT) users with a number of composite navigation signals, which are comprised of multiple binary (and, in some cases, multilevel) code-division multiple-access (CDMA) components on different carrier frequencies (Meurer & Antreich, 2017). The process of modulating signal components or CDMA waveforms onto a single carrier frequency is referred to as signal multiplexing. The simplest form of multiplexing is the combination of two bipolar components with the signal values –1 and +1 (e.g., legacy Global Positioning System [GPS] with coarse/acquisition [C/A] and P(Y) components at the L1 frequency), which is achieved by modulating one component in-phase (I) and the other in quadrature-phase (Q) to each other. This method maintains a constant envelope for the resulting complex waveform. The combination of at least three signal components requires the implementation of more sophisticated multiplexing schemes to ensure preservation of the constant-envelope property, which corresponds to the complex composite signal having a peak-to-average power ratio (PAPR) of 1 or 0 dB. The application of a constant-envelope signal to a high-power amplifier (HPA) enables the amplifier to operate in an efficient manner near its saturation point, thereby reducing the output power back-off (OBO) while simultaneously minimizing phase distortion

(Katz et al., 2016). Hence, the most common method in GNSSs is constant-envelope multiplexing (CEM), in which the navigation signals, along with intermodulation (IM) terms, are designed to form a constant-envelope composite signal, which is then fed into the satellite's HPA. The deployment of CEM enables the multiplexing technique and the HPAs to be conceived as two standalone building blocks within the signal transmission chain, where the input signal to the HPA is defined as a constant-envelope signal. This approach eliminates the necessity for detailed knowledge of the HPA and other payload characteristics.

In their book, Yao and Lu (2021) provide a comprehensive overview of CEM schemes. Selected CEM techniques proposed and used in the context of GNSSs include, for instance, quadrature phase-shift keying (QPSK), interplex (Butman & Timor, 1972), majority voting (MV) (Spilker & Orr, 1998), alternative BOC (AltBOC) (Lestarquit et al., 2008), phase-optimized constant-envelope transmission (POCET) (Dafesh & Cahn, 2009), and constant-envelope multiplexing via IM construction (CEMIC) (Yao, Guo, et al., 2017). In recent decades, the incorporation of additional signal components to accommodate an expanding array of services has fueled the development and refinement of CEM schemes. While there are examples of multicarrier systems, such as those developed by Dafesh and Cahn (2011), Won et al. (2011), Yao, Guo, et al. (2017), Yao, Ma, et al. (2017), and Nardin et al. (2023), multiplexing schemes are designed to achieve efficient transmission of multiple navigation signals on a single carrier, even when the composite multiplexed signal is composed of multiple frequency components.

The aforementioned multiplexing schemes share a commonality in that they derive IM terms in addition to a linear combination of N specified signal components, with the objective of ensuring the generation of a constant-envelope composite signal. To classify multiplexing methods, it is useful to identify whether the IM terms are defined as a set of equations with all signal components as input parameters. Alternatively, one might consider whether the values of the IM terms are the result of optimization based on all signal components as input. The former class could be designated as equation-based multiplexing (EBM), whereas the latter class could be designated as optimization-based multiplexing (OBM).

QPSK is one of the most straightforward EBM techniques, with one binary signal is transmitted in the I-component and one in the Q-component (Butman & Timor, 1972). With the formulation of interplex, Butman and Timor (1972) provided an updated EBM technique that introduces IM components based on a multiplication of the primary waveform with all other components. The first proposals of MV were EBM techniques, as MV constructs the IM term for an odd number of binary spreading waveforms according to the MV rationale (Allen et al., 2020; Spilker & Orr, 1998). With AltBOC, Lestarquit et al. (2008) established an EBM technique that generates one constant-envelope signal based on four binary waveforms by using a sub-carrier signal and constructing the necessary IM term with a closed-form expression, resulting in a signal with two spectral main lobes. Dafesh and Cahn (2009) proposed POCET, an OBM technique, which generates a phase lookup table (LUT) for binary spreading waveforms by minimizing the total transmit power while achieving fixed component signal powers and phase differences between each component. CEMIC is a flexible OBM technique that constructs a phase LUT for binary and even infinite bandwidth multilevel coded spreading symbol (MCS) waveforms by applying an IM construction algorithm requiring the power distribution of the signal components and the sampled spreading waveforms on a uniform time grid (Ma et al., 2019; Yao, Guo, et al., 2017; Yao & Lu, 2017).

As Katz et al. (2023) have outlined, the combination of CEM with an HPA pre-distortion linearizer (Katz et al., 2016) represents the prevailing approach to signal multiplexing when the HPA behavior is not ideal and applies nonlinear distortion to the signal. However, the power-sharing utilized for the generation and transmission of IM terms to construct a constant-envelope composite signal represents a multiplexing loss, as the IM terms are not usable by standard GNSS receivers. The IM terms do not provide ranging capabilities or carry navigation data, while simultaneously limiting the available power of the signal components that can be utilized for navigation. In many instances, these signals are filtered out by the payload's output multiplexer (OMUX) filter and antenna. For EBM interplex (Butman & Timor, 1972), the number of IM terms and the multiplexing loss increases rapidly with the number of components N to be multiplexed when one attempts to offer more services on the same carrier. Completely omitting IM terms may lead to zero multiplexing loss, but also results in signal deformations in the input amplitude to output amplitude (AM/AM) and input amplitude to output phase (AM/PM) caused by the payload's nonlinear HPA.

As an alternative to applying CEM in combination with an HPA pre-distortion linearizer, one could optimize the multiplexing scheme subject to a specific HPA model or parameter by relaxing the constant-envelope constraint. This process results in a OBM technique that shapes the signal constellation such that it no longer has a strictly constant envelope but has only a slight deviation and thus may be viewed as a form of the quasi-constant-envelope multiplexing (QCEM) technique (Vergara & Antreich, 2013). It has been shown that the scheme known as scalable interplex can increase the correlator output power at the receiver by transmitting only a fraction of the IM terms through the constant-envelope constraint (Vergara et al., 2013). Instead of considering multiplexing efficiency as an isolated figure of merit, Vergara et al. (2013) aimed to maximize the sum of correlator output powers of all signal components subject to an HPA model, termed the "receiver power efficiency." A study by Vergara and Antreich (2013) demonstrated a 10% receiver power efficiency gain despite signal deformations, when using scalable interplex rather than standard interplex, with the Galileo E1 signals as a case study, implemented as a five-channel interplex. In a study conducted by Ortega et al. (2020), the feasibility of incorporating a new bipolar signal, which may be designated as a fast acquisition signal, into the existing first-generation Galileo E1B, E1C, and public regulated service (PRS) components was investigated. The findings of this study led to the development of a modified version of CEMIC, designated ACEMIC. Furthermore, Ortega Espluga et al. (2020) published a mathematical development of the six-channel interplex ($N = 6$), which is a written formulation of the generalized form of the N-channel interplex formulas published by Vergara et al. (2013). The objective of Ortega et al. (2020) was to optimize the multiplexing of the first-generation Galileo E1 signals, which are represented by five bipolar spreading waveforms, as demonstrated by Vergara and Antreich (2013), with an additional bipolar spreading waveform for rapid acquisition. The proposed ACEMIC method is a form of QCEM, as it relaxes the constant-envelope constraint, and optimizing the LUT of CEMIC for a chosen joint PAPR metric results in an increased multiplexing efficiency, increasing from 0.7690 in the base to 0.8808 in the proposed ACEMIC configuration.

Therefore, the deployment of QCEM instead of CEM could enhance the received power level for numerous existing GNSS navigation signals, albeit with an increased susceptibility to HPA distortion. In light of the planned integration of additional signals into existing GNSS systems (Wallner et al., 2021), a QCEM approach could prove an effective means for mitigating or avoiding degradation of the ranging performance of already broadcast navigation signals resulting from the need for an over-proportionately higher power share of IM terms to maintain a constant envelope while introducing new services. The aforementioned QCEM methods optimize the signal constellation with respect to a power metric, rather than a distortion-sensitive ranging performance metric. It is not yet clear to what extent an increase in receiver power would also result in an improved ranging performance for each signal component. It is possible that an increase in HPA distortion might counteract these gains by adversely deforming the cross correlation function (CCF). In a previous study, we investigated the potential of scalable interplex for the Galileo E1 with an added signal component using the four-channel interplex as an approximation (Beck et al., 2022b) and assuming a Rapp-HPA characteristic (Rapp, 1991).

In this study, we assess the ranging performance of higher-order scalable interplex ($N \geq 5$), as proposed by Vergara and Antreich (2013). This approach aims to optimize the joint receiver efficiency for all signal components for given HPA characteristics. For optimized scalable interplex parameters, we analyze two key metrics: civil signal power recovery and achievable time of arrival (TOA) estimation error standard deviation (SD), a measure of the code tracking jitter. The evaluation of the TOA estimation error SD will employ an expression introduced by Vergara et al. (2019). This expression assesses not only the reception power but also the steepness of the distortion-affected CCF at the biased CCF main peak for a fixed early-late correlator spacing. This paper attempts to investigate the relationship between low multiplexing losses at the HPA input and low OBO at the HPA for a selected set of GNSS signals. As in the study conducted by Ortega et al. (2020), we consider the current Galileo E1 signal with one additional signal and model the multiplexing as a six-channel interplex. Differing from the work by Ortega et al. (2020), we investigate the multiplexing with a non-constant-envelope waveform as the additional signal component, which may be a suitable choice for receivers in the mass market (Beck et al., 2022a). In contrast to the approach taken by Beck et al. (2022b), a series of Saleh-HPA characteristics with varying OBO around a fixed input power will be employed as memory-less HPA models. The results indicate not only that scalable interplex can provide signals with increased reception power in the majority of cases but also that the influence of HPA distortions when applying QCEM instead of CEM does not adversely affect the code tracking jitter.

2 | SYSTEM MODEL

This section provides an overview of the system model and introduces each building block used in this study. Each building block will be represented by a complex function.

2.1 | Overview

In satellite navigation, it is common practice to generate one composite complex navigation signal generated with N signal components (also referred to as spreading waveforms in the context of CDMA). The n-th spreading waveform is given as follows:

$$x_n(t) = \sum_{m=-\infty}^{\infty} c_n(mT_{c,n}) p_n(t - mT_{c,n}) \qquad n \in \{1, 2, \ldots, N\} \tag{1}$$

This waveform is generated with a dedicated binary ranging code (and possibly also data) sequence $c_n(mT_{c,n}) \in \{+1, -1\}$, pulse shape $p_n(t - mT_{c,n})$, and spreading code chip duration $T_{c,n} = 1/f_{c,n}$. All signal components $x_n(t)$ are modulated by the

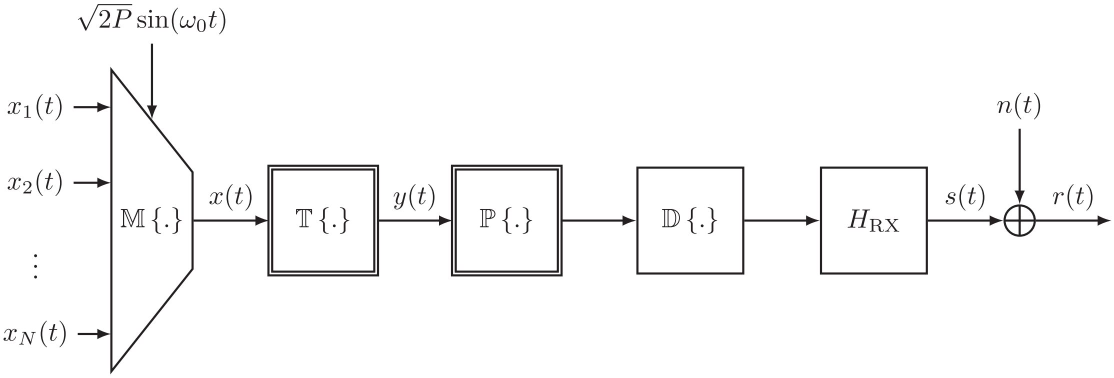

FIGURE 1 System model simulating the navigation signal from signal generation, payload distortion, channel propagation, receiver front-end filtering, and additive noise

input multiplexer (IMUX), which is represented by the complex function $\mathbb{M}\{.\}$, to a composite complex signal:

$$x(t) = \mathbb{M}\left\{(x_1(t), x_2(t), \ldots, x_N(t))\right\} \tag{2}$$

onto the same carrier frequency $f_0 = \omega_0/2\pi$. In most cases, the IMUX adds IM terms to avoid large HPA distortion while operating the HPA close to its saturation point. The multiplexed signal $x(t)$ is then fed to the transmit chain $\mathbb{T}\{.\}$ consisting of the nonlinear satellite HPA, OMUX, and antenna, resulting in the amplified and radiated complex signal:

$$y(t) = \mathbb{T}\{x(t)\} \tag{3}$$

The resulting transmit passband signal $y(t)$ is subsequently affected by the propagation channel $\mathbb{P}\{.\}$, resulting in the signal $\mathbb{P}\{y(t)\}$. The received passband signal is down-converted in the receiver to baseband, and the resulting signal is denoted by $\mathbb{D}\{\mathbb{P}\{y(t)\}\}$. The receiver front-end filtering is modeled with a linear filter $h_{\mathrm{RX}}(t)$. Thermal receiver noise is modeled as a complex additive white Gaussian noise (AWGN) process $n(t)$, whose real and imaginary parts are independent processes each with two-sided power spectral density (PSD) $N_0/2$. Thus, the analog complex baseband received signal is as follows:

$$r(t) = h_{\mathrm{RX}}(t) * \mathbb{D}\left\{\mathbb{P}\left\{y(t)\right\}\right\} + n(t) \triangleq s(t) + n(t) \tag{4}$$

where $*$ denotes the convolution operator. The received signal can then be represented as the sum of $s(t)$, which denotes the noise-free, but distorted satellite signal on the ground, and $n(t)$, which is the complex baseband AWGN. Figure 1 provides an overview of the navigation signal formation for the introduced system model. The following subsections elaborate on the models and assumptions applied to each building block within the simulation pipeline.

2.2 | Signal Components

The large increase in the use of GNSSs in mass-market devices over the last decade has further fostered the idea of providing additional Galileo signals in the E1 band. These added signals or services might be specifically tailored to low-complexity receivers (Wallner et al., 2020, 2021), as the Galileo E1 open service has been shown to induce high complexity in GNSS receivers, demanding a significantly higher bandwidth and memory than GPS owing to its modulation, long spreading sequences, and used memory spreading range codes that cannot be generated by shift registers.

Hence, in the following, we consider four Galileo services to investigate the potential of IM term scaling when attempting to add an additional signal component to the already existing three Galileo E1 services. The current Galileo E1 signal is comprised of three services, with one service being binary offset carrier (BOC)-modulated and two being composite binary offset carrier (CBOC)-modulated and multiplexed to one constant-envelope signal (Rebeyrol et al., 2006). In a previous study, the scalable interplex with an added Galileo E1 signal was modeled as a four-channel interplex with the three previously mentioned components and a signal candidate (Beck et al., 2022b).

However, this approach leads to approximation errors that can be avoided by modeling the Galileo E1 signal as a result of a five-channel interplex, as proposed by Vergara et al. (2013). Hence, in this study, the first five signal components are modeled such that they represent the three existing Galileo services in the E1 band. The additional spreading waveform is a signal candidate tailored to low-end receivers (Enneking et al., 2022) and was investigated by Beck et al. (2022b) as a potential signal candidate for receivers with a relatively narrow reception bandwidth. The naming conventions and properties of the investigated signal components are described as follows:

1. $\mathrm{BOC_{cos}}$-R(15, 2.5) is the first signal component. This component is BOC-modulated and cosine-phased and has a rectangular (R) pulse shape. The sub-carrier rate is $f_{\mathrm{sc},1} = 15 \times 1.023$ MHz, and the keying or chipping rate is $f_{\mathrm{chip},1} = 2.5 \times 1.023$ MHz. This BOC-modulation can be described via $p_1(t) = h_{\mathrm{BOC}}(t, f_{\mathrm{sc},1}, f_{\mathrm{chip},1}, \cos(.))$ with the following expression:

$$h_{\mathrm{BOC}}(t, f_{sc}, f_c, g(.)) = \begin{cases} \mathrm{sgn}(g(2\pi f_{sc} t)) & 0 \le t < 1/f_c \\ 0 & \text{else} \end{cases} \tag{5}$$

   where sgn(.) denotes the sign function (Meurer & Antreich, 2017). This signal component is called E1A and is the signal of the Galileo PRS.
2. $\mathrm{BOC_{sin}}$-R(1, 1) is the second signal component. The sub-carrier rate is $f_{\mathrm{sc},2} = 1 \times 1.023$ MHz, and the chipping rate is $f_{\mathrm{chip},2} = 1 \times 1.023$ MHz. The power ratio between the second and fourth component is 10 : 1, and the resulting pulse shape is $p_2(t) = h_{\mathrm{BOC}}(t, f_{\mathrm{sc},2}, f_{\mathrm{c},2}, \sin(.))$.
3. $\mathrm{BOC_{sin}}$-R(1, 1) is the third signal component. The sub-carrier rate is $f_{\mathrm{sc},3} = 1 \times 1.023$ MHz, and the chipping rate is $f_{\mathrm{c},3} = 1 \times 1.023$ MHz. The power ratio between the third and fifth component is 10 : 1, and the resulting pulse shape is $p_3(t) = h_{\mathrm{BOC}}(t, f_{\mathrm{sc},3}, f_{\mathrm{chip},3}, \sin(.))$.
4. $\mathrm{BOC_{sin}}$-R(6, 1) is the fourth signal component and is BOC-modulated. The sub-carrier rate is $f_{\mathrm{sc},4} = 6 \times 1.023$ MHz, and the chipping rate is $f_{\mathrm{c},4} = 1 \times 1.023$ MHz. The resulting pulse shape is $p_4(t) = h_{\mathrm{BOC}}(t, f_{\mathrm{sc},4}, f_{\mathrm{c},4}, \sin(.))$. The second and fourth components have the same ranging code and are modulated in-phase to each to other such that $\sqrt{10/11}p_2(t) + \sqrt{1/11}p_4(t)$ forms a $\mathrm{CBOC_{sin}}$-R(6, 1, 1/11, +), which corresponds to the Galileo E1B service.
5. $\mathrm{BOC_{sin}}$-R(6, 1) is the fifth signal component. The sub-carrier rate is $f_{\mathrm{sc},5} = 6 \times 1.023$ MHz, and the chipping rate is $f_{\mathrm{c},5} = 1 \times 1.023$ MHz.

The resulting pulse shape is $p_5(t) = h_{\mathrm{BOC}}(t, f_{\mathrm{sc},5}, f_{\mathrm{c},5}, \sin(.))$. The third and fifth components have the same ranging code and are modulated in anti-phase such that $\sqrt{10/11}p_3(t) - \sqrt{1/11}p_5(t)$ forms a CBOC$_{\sin}$-R(6, 1, 1/11,–), which corresponds to the Galileo E1C service.

6. BPSK-RC(1, 0.22) is the sixth signal component and is binary phase-shift keying (BPSK)-modulated with a keying rate of $f_{\mathrm{c},6} = 1/T_{\mathrm{c},6} = 1 \times 1.023$ MHz. The pulse is shaped with a raised-cosine (RC) with a roll-off factor of $\upsilon = 0.22$. The pulse shape is $p_6(t) = h_{\mathrm{RC}}(t/T_{\mathrm{chip},6}, 0.22)$ with the following expression:

$$h_{RC}(t,\upsilon) = \left(1 - \frac{\upsilon}{4}\right)^{-\frac{1}{2}} \frac{\cos(\pi\upsilon t)}{1-(2\upsilon t)^2} \frac{\sin(\pi t)}{\pi t} \tag{6}$$

as used in the Universal Mobile Telecommunications System (Proakis, 2001). This waveform is an example of a design tailored to receivers with a relatively low sampling rate and, consequently, a small receiver filtering bandwidth. The motivation for deploying such a signal would be to minimize filtering losses along the signal propagation path in order to maximize the signal-to-noise ratio (SNR) for users (Beck et al., 2022a). It can be argued that this signal is not necessarily an optimal tracking signal, owing to the fact that the auto-correlation function (ACF) is relatively smooth, which results in a larger TOA estimation error SD than a BPSK-R(1) waveform, such as the GPS L1 C/A signal. Moreover, the waveform itself is not a constant-envelope signal, which introduces additional complexities to the multiplexing process. Hence, there is a scarcity of robust multiplexing techniques capable of handling this type of signal as an input. For these reasons, the BPSK-RC(1, 0.22) was deemed unsuitable for the first generation of Galileo signals (Ávila Rodríguez, 2008). Nevertheless, a BPSK-RC(1, 0.22) signal could prove to be an effective acquisition signal, especially for the majority of GNSS receivers currently available in the low-end mass-market segment. These receivers are typically constrained in their power consumption and, therefore, rarely perform tracking for extended periods of time. Instead, these receivers primarily perform duty-cycled acquisition in order to determine a PNT solution (Enneking et al., 2022).

In the following investigation, the Galileo E1 signal will be generated as a six-channel interplex, but the TOA estimation error SD will be evaluated by using four replicas that correspond to the services currently transmitted by Galileo, including the added component. These replicas are as follows:

$$\bar{x}_1(t) = x_1(t) \tag{7a}$$

$$\bar{x}_2(t) = \sqrt{\frac{10}{11}}x_2(t) + \sqrt{\frac{1}{11}}x_4(t) \tag{7b}$$

$$\bar{x}_3(t) = \sqrt{\frac{10}{11}}x_3(t) - \sqrt{\frac{1}{11}}x_5(t) \tag{7c}$$

$$\bar{x}_4(t) = x_6(t) \tag{7d}$$

which will be used to evaluate the ACFs and CCFs. Figure 2 illustrates the PSDs of the signal replicas.

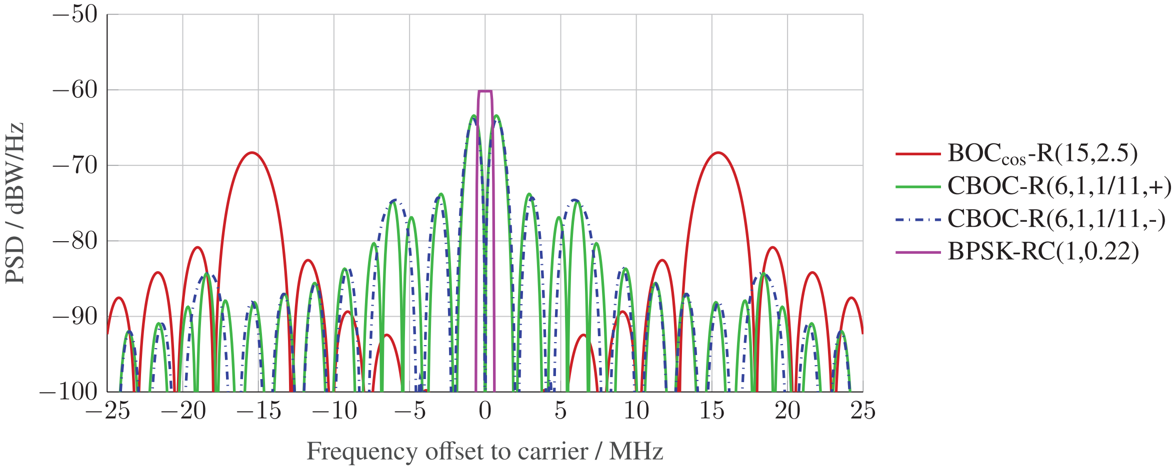

FIGURE 2 PSDs of the signal replicas

2.3 | Multiplexing

This paper focuses on scalable interplex, which is a modified version of the N-channel interplex, as described by Butman and Timor (1972). The N-channel interplex is a phase modulation (PM) system resulting in the following composite signal:

$$x(t) = \mathbb{M}\{x_1(t), x_2(t), \cdots, x_N(t)\} = \sqrt{2P^{(N)}}\sin\left(\omega_0 t + \Theta(t)\right) \tag{8}$$

where $P^{(N)}$ denotes the total mean power, ω_0 denotes the angular carrier frequency, and $\Theta(t)$ denotes the PM term, which requires N spreading waveforms and N modulation angles as input. The PM term for the N-channel interplex is as follows:

$$\begin{aligned}\Theta(t) &= \left(\theta_1 + \sum_{n=2}^{N}\theta_n x_n(t)\right)x_1(t)\\ &= \theta_1 x_1(t) + \theta_2 x_2(t)x_1(t) + \theta_3 x_3(t)x_1(t) + \cdots + \theta_n x_n(t)x_1(t)\end{aligned} \tag{9}$$

with θ_1, …, θ_N denoting the modulating angles, which essentially determine the power distribution of the input waveforms and the implicitly generated IM terms when the input waveforms are power-normalized. Furthermore, the value range of the modulation angles is relevant to the correct generation of the composite CBOC$_{\text{sin}}$-R(6, 1, 1/11, +) and CBOC$_{\text{sin}}$-R(6, 1, 1/11,–) waveforms, as $\pi < \theta_n < 2\pi$ causes a polarity flip of the respective signal component n with respect to the primary component if and only if $\theta_1 = \pi/2$. The N-channel interplex reduces the power dissipated in the IM terms already in a two-component setup compared with QPSK. When introducing the N-channel interplex with a sine carrier, it is helpful to set the modulation angle $\theta_1 = \pi/2$ of the primary waveform $x_1(t)$, as it collapses the number of IM terms $N_{\text{IM}} = 2^{N-1} - N$ (Vergara et al., 2013). The CEM of the Galileo E1B, E1C, and PRS signals on the E1 carrier, as described by Rebeyrol et al. (2006), can be represented as a five-channel interplex of the respective five bipolar sub-components with a target power ratio of 2:1 between PRS and E1B and 1:1 between E1B and E1C (Vergara & Antreich, 2013). Thus, the use of eleven IM terms is necessary for the Galileo E1 multiplex when the five-channel interplex analogy is applied. To minimize the influence of approximation errors when inspecting the Galileo E1 signal with an added non-binary component, a six-channel interplex is used to derive the scalable interplex formulation, as, for instance, reported by Ortega et al. (2020). The six-channel interplex can be given as follows:

$$x(t)=\sqrt{2P^{(6)}}\,\sin\left(\begin{array}{l}\omega_0 t+\theta_1 x_1(t)+\theta_2 x_2(t)x_1(t)+\theta_3 x_3(t)x_1(t)\\ +\theta_4 x_4(t)x_1(t)+\theta_5 x_5(t)x_1(t)+\theta_6 x_6(t)x_1(t)\end{array}\right) \tag{10}$$

which is referred to in the latter as the standard six-channel interplex.

The main idea for yielding a scalable interplex expession starting with Equation (10) is the application of trigonometric identities, as shown in Appendix A, such that the reformulated expression is a sum of products of the sine and cosine of the modulation angles and a product of the signal components. Each additive term that contains only one single signal component $x_n(t)$ is a useful signal term. All other terms that contain a product of signal components are designated as IM terms, constituting the complex IM component (i.e., complex sum of all IM terms). A generalized expression for yielding this additive expression for any N-channel interplex was developed by Vergara et al. (2013). We note that Ortega Espluga et al. (2020) published a written formulation of this expression for the six-channel interplex when a cosine carrier is selected. By using a sine carrier and setting $\theta_1=\pi/2$, waveforms from $x_2(t)$ to $x_N(t)$ are I-broadcast, whereas the primary component $x_1(t)$ is Q-transmitted. Setting the parameters as such, the scalable six-channel interplex can be expressed as follows:

$$x(t)=\sqrt{2P^{(6)}}\,\sin(\omega_0 t)I(t)+\sqrt{2P^{(6)}}\,\cos(\omega_0 t)Q(t) \tag{11}$$

with:

$$\begin{aligned}
I(t)=&-\sin(\theta_2)\cos(\theta_3)\cos(\theta_4)\cos(\theta_5)\cos(\theta_6)\,x_2(t) && \text{(Signal term 1)}\\
&+\sin(\theta_2)\cos(\theta_3)\cos(\theta_4)\sin(\theta_5)\sin(\theta_6)\,x_2(t)x_5(t)x_6(t)\,\kappa_{11} && \text{(IM term 11)}\\
&+\sin(\theta_2)\cos(\theta_3)\sin(\theta_4)\sin(\theta_5)\cos(\theta_6)\,x_2(t)x_4(t)x_5(t)\,\kappa_{13} && \text{(IM term 13)}\\
&+\sin(\theta_2)\cos(\theta_3)\sin(\theta_4)\cos(\theta_5)\sin(\theta_6)\,x_2(t)x_4(t)x_6(t)\,\kappa_{12} && \text{(IM term 12)}\\
&+\sin(\theta_2)\sin(\theta_3)\sin(\theta_4)\cos(\theta_5)\cos(\theta_6)\,x_2(t)x_3(t)x_4(t)\,\kappa_{16} && \text{(IM term 16)}\\
&-\sin(\theta_2)\sin(\theta_3)\sin(\theta_4)\sin(\theta_5)\sin(\theta_6)\,x_2(t)x_3(t)x_4(t)x_5(t)x_6(t)\,\kappa_1 && \text{(IM term 1)}\\
&+\sin(\theta_2)\sin(\theta_3)\cos(\theta_4)\sin(\theta_5)\cos(\theta_6)\,x_2(t)x_3(t)x_5(t)\,\kappa_{15} && \text{(IM term 15)}\\
&+\sin(\theta_2)\sin(\theta_3)\cos(\theta_4)\cos(\theta_5)\sin(\theta_6)\,x_2(t)x_3(t)x_6(t)\,\kappa_{14} && \text{(IM term 14)}\\
&-\cos(\theta_2)\sin(\theta_3)\cos(\theta_4)\cos(\theta_5)\cos(\theta_6)\,x_3(t) && \text{(Signal term 3)}\\
&+\cos(\theta_2)\sin(\theta_3)\cos(\theta_4)\sin(\theta_5)\sin(\theta_6)\,x_3(t)x_5(t)x_6(t)\,\kappa_8 && \text{(IM term 8)}\\
&+\cos(\theta_2)\sin(\theta_3)\sin(\theta_4)\sin(\theta_5)\cos(\theta_6)\,x_3(t)x_4(t)x_5(t)\,\kappa_{10} && \text{(IM term 10)}\\
&+\cos(\theta_2)\sin(\theta_3)\sin(\theta_4)\cos(\theta_5)\sin(\theta_6)\,x_3(t)x_4(t)x_6(t)\,\kappa_9 && \text{(IM term 9)}\\
&-\cos(\theta_2)\cos(\theta_3)\sin(\theta_4)\cos(\theta_5)\cos(\theta_6)\,x_4(t) && \text{(Signal term 4)}\\
&+\cos(\theta_2)\cos(\theta_3)\sin(\theta_4)\sin(\theta_5)\sin(\theta_6)\,x_4(t)x_5(t)x_6(t)\,\kappa_7 && \text{(IM term 7)}\\
&-\cos(\theta_2)\cos(\theta_3)\cos(\theta_4)\sin(\theta_5)\cos(\theta_6)\,x_5(t) && \text{(Signal term 5)}\\
&-\cos(\theta_2)\cos(\theta_3)\cos(\theta_4)\cos(\theta_5)\sin(\theta_6)\,x_6(t) && \text{(Signal term 6)}
\end{aligned} \tag{12}$$

and:

$$\begin{aligned}
Q(t) = {} & +\cos(\theta_2)\cos(\theta_3)\cos(\theta_4)\cos(\theta_5)\cos(\theta_6)\,x_1(t) && \text{(Signal term 1)} \\
& \cos(\theta_2)\cos(\theta_3)\cos(\theta_4)\sin(\theta_5)\sin(\theta_6)\,x_1(t)\,x_5(t)\,x_6(t)\,\kappa_{17} && \text{(IM term 17)} \\
& -\cos(\theta_2)\cos(\theta_3)\sin(\theta_4)\sin(\theta_5)\cos(\theta_6)\,x_1(t)\,x_4(t)\,x_5(t)\,\kappa_{19} && \text{(IM term 19)} \\
& -\cos(\theta_2)\cos(\theta_3)\sin(\theta_4)\cos(\theta_5)\sin(\theta_6)\,x_1(t)\,x_4(t)\,x_6(t)\,\kappa_{18} && \text{(IM term 18)} \\
& -\cos(\theta_2)\sin(\theta_3)\sin(\theta_4)\cos(\theta_5)\cos(\theta_6)\,x_1(t)\,x_3(t)\,x_4(t)\,\kappa_{22} && \text{(IM term 22)} \\
& +\cos(\theta_2)\sin(\theta_3)\sin(\theta_4)\sin(\theta_5)\sin(\theta_6)\,x_1(t)\,x_3(t)\,x_4(t)\,x_5(t)\,x_6(t)\,\kappa_2 && \text{(IM term 2)} \\
& -\cos(\theta_2)\sin(\theta_3)\cos(\theta_4)\sin(\theta_5)\cos(\theta_6)\,x_1(t)\,x_3(t)\,x_5(t)\,\kappa_{21} && \text{(IM term 21)} \\
& -\cos(\theta_2)\sin(\theta_3)\cos(\theta_4)\cos(\theta_5)\sin(\theta_6)\,x_1(t)\,x_3(t)\,x_6(t)\,\kappa_{20} && \text{(IM term 20)} \\
& -\sin(\theta_2)\sin(\theta_3)\cos(\theta_4)\cos(\theta_5)\cos(\theta_6)\,x_1(t)\,x_2(t)\,x_3(t)\,\kappa_{26} && \text{(IM term 26)} \\
& +\sin(\theta_2)\sin(\theta_3)\cos(\theta_4)\sin(\theta_5)\sin(\theta_6)\,x_1(t)\,x_2(t)\,x_3(t)\,x_5(t)\,x_6(t)\,\kappa_4 && \text{(IM term 4)} \\
& +\sin(\theta_2)\sin(\theta_3)\sin(\theta_4)\sin(\theta_5)\cos(\theta_6)\,x_1(t)\,x_2(t)\,x_3(t)\,x_4(t)\,x_5(t)\,\kappa_6 && \text{(IM term 6)} \\
& +\sin(\theta_2)\sin(\theta_3)\sin(\theta_4)\cos(\theta_5)\sin(\theta_6)\,x_1(t)\,x_2(t)\,x_3(t)\,x_4(t)\,x_6(t)\,\kappa_5 && \text{(IM term 5)} \\
& -\sin(\theta_2)\cos(\theta_3)\sin(\theta_4)\cos(\theta_5)\cos(\theta_6)\,x_1(t)\,x_2(t)\,x_4(t)\,\kappa_{25} && \text{(IM term 25)} \\
& +\sin(\theta_2)\cos(\theta_3)\sin(\theta_4)\sin(\theta_5)\sin(\theta_6)\,x_1(t)\,x_2(t)\,x_4(t)\,x_5(t)\,x_6(t)\,\kappa_3 && \text{(IM term 3)} \\
& -\sin(\theta_2)\cos(\theta_3)\cos(\theta_4)\sin(\theta_5)\cos(\theta_6)\,x_1(t)\,x_2(t)\,x_5(t)\,\kappa_{24} && \text{(IM term 24)} \\
& -\sin(\theta_2)\cos(\theta_3)\cos(\theta_4)\cos(\theta_5)\sin(\theta_6)\,x_1(t)\,x_2(t)\,x_6(t)\,\kappa_{23} && \text{(IM term 23)}
\end{aligned} \tag{13}$$

Here, a scalar IM steering coefficient $\kappa_j \in [0, 1]$ is introduced for each IM term (Vergara et al., 2013). The introduction of the IM steering coefficients κ_j with $j \in \mathcal{I}_{\mathrm{IM}} = \{1, \ldots, 26\}$ allows the scaling of each IM term and therefore the shaping of the IM component and the whole signal constellation. This approach permits scalable interplex to modify the composite complex signal $x(t)$ considering an HPA realization, thereby reducing the power of the IM component while simultaneously increasing the power of the useful signal components. The first of the two extreme cases is $\kappa_j = 1\ \forall j \in \mathcal{I}_{\mathrm{IM}}$, which results in the scalable interplex being equal to the standard interplex when strictly bipolar spreading waveforms are used with $x_n(t) \in \{-1, +1\}$. In this case, the signal $x(t)$ has a constant envelope. In the case of non-bipolar, power-normalized spreading waveforms, Equation (11) with Equations (12) and (13) is an approximation of the standard interplex (Equation (10)). In this study, the utilization of the BPSK-RC(1, 0.22) waveform as $x_6(t)$, which is not a bipolar waveform, thus indicates that the scalable interplex employed is an approximation of the standard interplex even if $\kappa_j = 1\ \forall j \in \mathcal{I}_{\mathrm{IM}}$. The latter of the two extreme cases is the complete omission of IM terms, where $\kappa_j = 0\ \forall j \in \mathcal{I}_{\mathrm{IM}}$. This scenario results in severe HPA distortion and is not a desired configuration for any realistic HPA characteristic. In the latter, for the purpose of achieving a more compact notation, all IM steering coefficients are aggregated into a single vector, designated as follows:

$$\kappa = \begin{bmatrix} \kappa_1 & \kappa_2 & \cdots & \kappa_j \cdots & \kappa_{26} \end{bmatrix}^{\mathrm{T}} \in [0, 1]^{26\times 1} \tag{14}$$

The scalable interplex formulation (Equation (11)) with Equations (12) and (13) further allows one to chose a power distribution among the user signals by solving for the modulation angles $\theta_1, \ldots, \theta_N$. A key metric for CEM methods is the multiplexing efficiency:

$$\eta_{\mathrm{MUX}} = 1 - \frac{P_{\mathrm{IM}}}{P^{(N)}} \tag{15}$$

which assesses the power of unusable IM component P_{IM} over the average total signal power of the composite signal $x(t)$:

$$P^{(N)} = \sum_{n=1}^{N} P_n^{(N)} + P_{\mathrm{IM}} \tag{16}$$

where $P_n^{(N)}$ denotes the average power of the n-th signal component $x_n(t)$. A multiplexing method with $\eta_{\mathrm{MUX}} = 1$ allocates all signal power $P^{(N)}$ only to useful signal terms and therefore does not contain any IM terms. The N-channel interplex has the worst performance with respect to the multiplexing efficiency η_{MUX} if the modulation angles are chosen in such a way that the power of each signal component is equal, resulting in a uniform power distribution. This scenario causes the highest possible IM power (Butman & Timor, 1972) and therefore the lowest multiplexing efficiency η_{MUX}. Thus, an unevenness in the power distribution of the signal components is advantageous and is also realized with the Galileo E1 signals (Rebeyrol et al., 2006).

In the context of Galileo E1 with an additional component implemented as a six-channel interplex, similar to the work conducted by Ortega et al. (2020), it is simple to implicitly set the power distribution of the user signals and the IM power by choosing the following power ratios:

$$\alpha = \frac{P_1^{(6)}}{P_2^{(6)} + P_4^{(6)}} = \frac{P_1^{(6)}}{P_3^{(6)} + P_5^{(6)}} \tag{17}$$

and:

$$\beta = \frac{P_1^{(6)}}{P_6^{(6)}} \tag{18}$$

between the primary and other components. The fixed power ratio is given as follows:

$$10 = \frac{P_2^{(6)}}{P_4^{(6)}} = \frac{P_3^{(6)}}{P_5^{(6)}} \tag{19}$$

and is set to correctly construct the CBOC components given in the Galileo interface control document (ICD).

Owing to the non-discrete range of values inherent to a BPSK-RC(1, 0.22) waveform, a fair comparison between scalable interplex and a potent CEM method such as CEMIC would prove to be challenging. To illustrate this point, a case study could be conducted to compare the performance of scalable interplex with BPSK-RC(1, 0.22) and CEMIC with a discrete derivative of BPSK-RC(1, 0.22). For example, an MCS with 16, 32, or 64 sub-chips could be used as a discrete derivative of BPSK-RC(1, 0.22). This prompts the following question: With which replica would a receiver correlate such a signal? Assuming the implementation of a BPSK-RC(1, 0.22) waveform for low-complexity receivers would be advantageous, as employing an identical replica would inevitably result in a correlation loss due to replica mismatch for CEMIC, rendering this analysis potentially unfair. Consequently, a comparison of QCEM and CEM is beyond the scope of this paper.

2.4 | Transmitter

A model of a GNSS satellite transmitter $\mathbb{T}\{.\}$ may comprise an HPA, OMUX, and antenna model (Beck et al., 2022a). To solely investigate the interplay between the constellation shaping of the multiplexer when applying scalable interplex and the distortion introduced by the HPA, the effect of band limitations on the transmitter side was neglected in this paper. Hence, the OMUX and antenna were assumed to have an ideal all-pass characteristic without phase distortion such that the transmitter model effectively comprises only an HPA characteristic.

As there is no publicly available information on the detailed shape of GNSS satellite amplifier characteristics, a generic memory-less HPA model was used, which assumes a perfect HPA pre-distortion. The used HPA model is a Saleh model with AM/AM and AM/PM characteristics:

$$A(|x(t)|) = \frac{a_A|x(t)|}{1 + b_A|x(t)|^2} \tag{20a}$$

$$\vartheta(x(t)) = \operatorname{atan2}\Big(\operatorname{Im}\{x(t)\}, \operatorname{Re}\{x(t)\}\Big) \tag{20b}$$

where the two parameters a_A and $b_A = 1/|x_0|^2$ denote the small signal gain and the input amplitude $|x_0|$ at which the maximum output amplitude $A_0 = a_A/(2|x_0|)$ is achieved (Saleh, 1981). The formation of the transmit signal is as follows:

$$y(t) = \mathbb{T}\Big\{x(t)\Big\} = A(|x(t)|)e^{i\vartheta(x(t))} \tag{21}$$

corresponding to the application of AM/AM and AM/PM mappings onto the multiplexed input $x(t)$.

2.5 | Channel and Receiver Model

This paper considers only path loss in the propagation channel such that the satellite signal on the ground can be expressed as $\mathbb{P}\{y(t)\} = \gamma y(t - \tau_0)$, where $\gamma \in \mathbb{R}$ denotes the channel coefficient, which models the signal path loss, and $\tau_0 \in \mathbb{R}$ denotes the propagation delay. The receiver applies only frequency down-conversion and front-end filtering with a brick-wall filter $h_{\text{RX}}(t)$ such that the received signal can be expressed as $r(t) = h_{\text{RX}}(t) * \mathbb{D}\Big\{\gamma y(t - \tau_0)\Big\} + n(t)$. The effect of quantization lies beyond the scope of this paper.

3 | METHODOLOGY

This section describes the methodology employed in the study. Firstly, the performance metrics used to derive scalable interplex IM steering vectors and to evaluate the performance of this method in terms of signal power gain and ranging performance are presented. Secondly, the HPA and power distributions employed in the study are outlined. Finally, this section illustrates how IM steering vectors were derived for each HPA characteristic and user signal power setting.

3.1 | Performance Measures

This subsection presents the five performance metrics assessed in this study. The first metric is the joint receiver power efficiency, which serves as the objective of the scalable interplex optimization process. The latter four metrics are the civil signal power recovery, scalable interplex IM power ratio, joint receiver power efficiency gain, and TOA estimation error SD, which are used to evaluate the viability of scalable interplex in the chosen scenario.

3.1.1 | Joint Receiver Power Efficiency

Vergara and Antreich (2013) defined the joint receiver power efficiency as follows:

$$\eta_{\text{eff}}(\boldsymbol{\kappa}) = \frac{\sum_{n=1}^{6} z_n(\boldsymbol{\kappa})}{P_{\text{TX}}} \quad \in [0,1] \tag{22}$$

with:

$$z_n(\boldsymbol{\kappa}) = \begin{cases} \left| \dfrac{1}{T}\displaystyle\int_{\Pi} \text{Im}\{y(t,\boldsymbol{\kappa})\} x_1(t)\,dt \right|^2, & n = 1 \\ \left| \dfrac{1}{T}\displaystyle\int_{\Pi} \text{Re}\{y(t,\boldsymbol{\kappa})\} x_n(t)\,dt \right|^2, & n \in \{2,3,4,5,6\} \end{cases} \tag{23}$$

where $P_{\text{TX}} = \lim_{T\to\infty} \frac{1}{2T}\int_{-T}^{+T} |y(t)|^2 \, \mathrm{d}t$ denotes the total average output power of the HPA at its operation point and $\Pi = (-T_0/2, +T_0/2)$ denotes an observation window with observation time $T_0 > 0$. This metric assesses the prompt sum of correlation powers after the composite signal has passed through the HPA, with a particular focus on a signal in which the primary signal component ($n = 1$) is allocated to the Q-channel and the other components ($n \geq 2$) are allocated to the I-channel. In the case of undistorted constant-envelope signals, this metric is equivalent to the multiplexing efficiency η_{mux}. However, in the presence of distorted and/or non-constant-envelope signals, the joint receiver power efficiency η_{eff} is also subject to correlation losses resulting from the inherent distortion of the HPA. This metric serves as the objective for scalable interplex optimization, resulting in an IM coefficient for each IM term for a specific HPA characteristic (Vergara & Antreich, 2013). In the case of IM term omission, the maximum joint receiver power efficiency $\eta_{\text{eff}}(0) = 1$ can only be attained with an idealized HPA model that does not apply amplitude compression. In its current form, Equation (23) is not sensitive to range biases that might be induced from the AM/PM characteristic.

3.1.2 | *Civil Signal Power Recovery*

The introduction of additional signals for a given satellite payload would necessitate either an increase in transmit power to the extent permitted by the hardware or a reduction in the power of the components that are already being transmitted. The optimal scenario would be transmission of the additional signal without any degradation to existing services. However, increasing the number of signal components from an already higher-order multiplexing state with a greater number of IM than signal terms results in a disproportionate loss of signal reception power for the same transmit power if CEM is applied. An intriguing figure of merit for this scenario is the amount of reception power that could be recovered when the CEM constraint is relaxed by adopting a scalar interplex rather than a standard interplex approach. To assess the civil signal power loss using either type of scalable interplex, the Galileo E1B/C signal gain that occurs when a new signal component is added can be defined as follows:

$$G_{\text{opt}} = G(\boldsymbol{\kappa}_{\text{opt}}) = \frac{\dfrac{P_2^{(6)}(\boldsymbol{\kappa}_{\text{opt}}) + P_4^{(6)}(\boldsymbol{\kappa}_{\text{opt}})}{P^{(6)}}}{\dfrac{P_2^{(5)}(\boldsymbol{\kappa}_{\text{opt}}) + P_4^{(5)}(\boldsymbol{\kappa}_{\text{opt}})}{P^{(5)}}} = \frac{\dfrac{P_3^{(6)}(\boldsymbol{\kappa}_{\text{opt}}) + P_5^{(6)}(\boldsymbol{\kappa}_{\text{opt}})}{P^{(6)}}}{\dfrac{P_3^{(5)}(\boldsymbol{\kappa}_{\text{opt}}) + P_5^{(5)}(\boldsymbol{\kappa}_{\text{opt}})}{P^{(5)}}} \tag{24}$$

where $P_n^{(6)}(\boldsymbol{\kappa})$ is derived from a six-channel scalable interplex solution with a 26-dimensional IM steering vector $\boldsymbol{\kappa}_{\text{opt}}$. The civil signal power loss obtained when using the standard six-channel interplex is denoted as $\tilde{G}$.

3.1.3 | *Scalable Interplex IM Power Ratio*

In addition to the civil signal power recovery metric, which compares the states before and after the addition of a single new signal, one can also assess the reduction in IM power used when applying a six-channel scalable interplex instead of the standard six-channel interplex with the following variable:

$$v_{\text{opt}} = v(\boldsymbol{\kappa}_{\text{opt}}) = \frac{P_{\text{IM}}(\boldsymbol{\kappa}_{\text{opt}})}{\tilde{P}_{\text{IM}}} \triangleq \frac{P_{\text{IM,opt}}}{\tilde{P}_{\text{IM}}} \tag{25}$$

where the total power of all signal components $P^{(6)}$ is held constant, $\tilde{P}_{IM}$ denotes the power allocated to the IM component when standard interplex is applied, and $P_{\text{IM,opt}}$ denotes the power allocated to the IM component when scalable interplex is applied with an IM steering vector $\boldsymbol{\kappa}_{\text{opt}}$ derived in the scalable interplex optimization for a specific HPA characteristic.

3.1.4 | *Joint Receiver Power Efficiency Gain*

Similar to the scalable interplex IM power ratio, the joint receiver power efficiency gain is given as follows:

$$\zeta_{\text{opt}} = \zeta(\boldsymbol{\kappa}_{\text{opt}}) = \frac{\eta_{\text{eff}}(\boldsymbol{\kappa}_{\text{opt}})}{\tilde{\eta}_{\text{eff}}} \tag{26}$$

and quantifies the enhancement in joint receiver efficiency when a six-channel scalable interplex is employed in comparison to the standard six-channel interplex. Here, $\tilde{\eta}_{\text{eff}}$ denotes the joint receiver efficiency of the standard interplex, and $\eta_{\text{eff}}(\boldsymbol{\kappa}_{\text{opt}})$ indicates the joint receiver efficiency of the scalable interplex solution with the IM steering vector $\boldsymbol{\kappa}_{\text{opt}}$ derived in the scalable interplex optimization for a specific HPA characteristic.

3.1.5 | *TOA Estimation Error SD*

The unsmoothed TOA estimation error SD for a code phase that assumes AWGN for a fixed early-late correlator spacing Δ was derived by Betz and Kolodziejski (2009) and later generalized for the case in which the received navigation signal and the respective signal replica do not match (Vergara et al., 2019). Casting their results in the time domain leads to the TOA estimation error SDs, for $i \in \{1, 2, 3, 4\}$:

$$\sigma_{\tau,i}(\Delta) = \sqrt{\frac{N_0}{2E_s} \frac{(1-\rho_{\bar{x}_i}(\Delta))/2}{\left(\rho'_{s\bar{x}_i}(\Delta/2)\right)^2}} \tag{27}$$

where the variables are defined below. Within the observation time window Π, we have the following:

$$\rho_{\bar{x}_i}(\tau) = \int_{\Pi} \bar{x}_i(t-\tau)\bar{x}_i(t)\,\mathrm{d}t, \quad i \in \{1,2,3,4\} \tag{28}$$

which denotes the ACF of the i-th replica, normalized to $\rho_{\bar{x}_i}(0) = 1$. Additionally, the energy of the distorted satellite signal on the ground $s(t)$ is given as follows:

$$E_s = \int_{\Pi} |s(t)|^2\,\mathrm{d}t \tag{29}$$

We have the following expression:

$$\rho_{s\bar{x}_i}(\tau) = \frac{1}{\sqrt{E_s}} \int_{\Pi} s(t-\tau)\,\bar{x}_i(t)\,\mathrm{d}t \tag{30}$$

which denotes the normalized CCF of the distorted satellite signal on the ground $s(t)$ and the i-th signal replica $\bar{x}_i(t)$. The derivative of this function is denoted by $\rho'_{s\bar{x}_i}(\tau) \triangleq \frac{d}{d\tau}\rho_{s\bar{x}_i}(\tau)$.

3.2 | Configuration of Signal Power Distribution and Amplifier Operating Region

This study examines two distinct six-channel interplex operating states, which will henceforth be designated as power modes. The power modes are distinguished by differing values of the power ratio β, which represents the power ratio of the first to the sixth signal component. The modulation angles are essentially determined by the defined power ratios α and β among the user signals and their polarity with respect to each other. The selected power modes result in varying levels of baseline multiplexing efficiency η_{MUX}, as detailed in Table 1. Power ratios between signal components of a similar scale can be found for GPS (Thölert et al., 2018) and Galileo signals (Rebeyrol et al., 2006). In power mode I, it is assumed that the additional signal has the same power as the E1B and E1C signals that are already broadcast. In power mode II, the additional signal is assumed to have a power level equal to 1/3 of that of the PRS signal or 2/3 of that of the E1B signal. The power ratio $\alpha = 2$ between PRS and each already present open service signal is as in the Galileo ICD and achieved by the Galileo E1 signal multiplex described by Rebeyrol et al. (2006).

Three scenarios are investigated for which the HPA was driven in either its saturation, transition, or linear region. To facilitate a fair comparison of ranging performances for different HPA operation regions, the small signal gain a_A and maximum output amplitude A_0 were chosen such that an operating point with an input power of 0 dBW (= 1 W) would result in the same HPA output power of $P_{\text{TX}} = 15.5$ dBW (≈ 35.5 W). This scenario was achieved by setting the maximum output amplitude A_0 such that a certain OBO is attained and then solving for the small signal gain a_A. Table 2 shows the applied parameters for the three realistic HPA models and an additional idealized HPA model. The fourth HPA is a theoretical example of an HPA with idealized amplification (i.e., linear amplification with a_A and no amplitude compression). This HPA characteristic is used as a reference, as any realistic Saleh-HPA model imposes an implicit average power constraint. An overly severe down-scaling of IM terms can deteriorate the joint receiver efficiency metric as correlation losses occur, owing to a mismatch in the received signal and signal replica. Nevertheless, an idealized HPA model permits the complete omission of IM terms, as amplitude compression does not occur. Consequently, the results yielded by this model indicate the upper or lower limits that can be achieved, depending on the metric in question. The corresponding AM/AM characteristics for each HPA model and the common operation point are shown in the amplitude domain in Figure 3.

TABLE 1

Power Modes and Their Respective Modulation Angles in Degrees and Multiplexing Efficiencies for the Standard Six-Channel Interplex

Power mode	α	β	θ_1	θ_2	θ_3	θ_4	θ_5	θ_6	$\tilde{P}_{\text{IM}}/P^{(6)}$	η_{MUX}
I	2	2	90.00	326.01	33.99	347.96	347.96	324.74	27.93%	72.07%
II	2	3	90.00	326.01	33.99	347.96	347.96	330.00	24.32%	75.68%

TABLE 2

HPA Modeling Parameters

HPA model	Operation region	a_A	b_A /W–1	OBO / dB
1	saturation region	11.074	0.8591	0.0250
2	transition region	8.1962	0.3760	1.0000
3	linear region	6.9821	0.1721	3.0000
4	linear region	5.9566	0.0000	∞

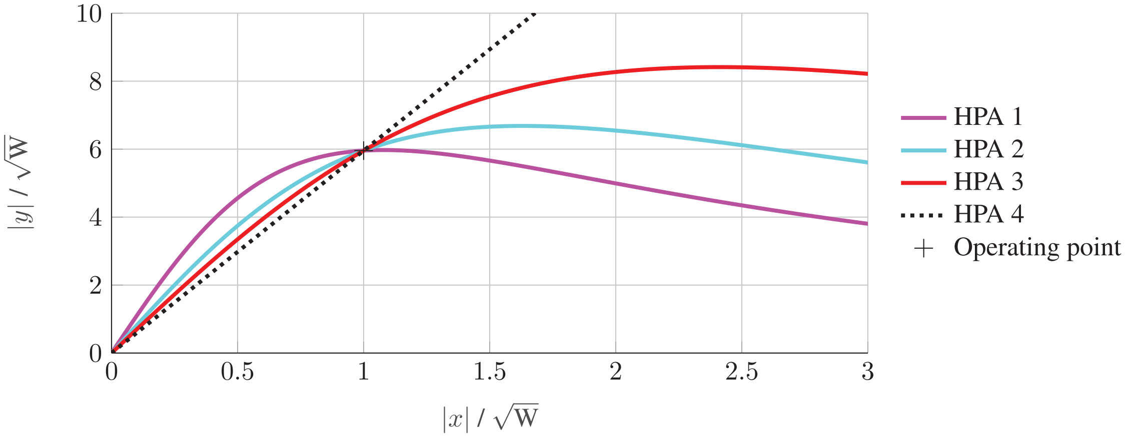

FIGURE 3 AM/AM mappings of applied HPA models

3.3 | Optimization of Scalable Interplex IM Steering Vectors

Vergara and Antreich (2013) presented the scalable five-channel interplex as a two-dimensional optimization problem (OP), with the variables being the IM steering coefficients for all I-IM terms and Q-IM terms, which reduces the computational complexity but scales IM terms with less granularity. To ascertain the full potential of scalable interplex, this paper employs a refined approach and aims to optimize the IM steering coefficient of each IM term individually. The refined scalable six-channel interplex OP is 26-dimensional, as there exist a total of 26 IM steering coefficients, as shown in Equations (12) and (13). The OP can then be expressed as follows:

$$\begin{aligned} \max_{\boldsymbol{\kappa}} \quad & \eta_{\text{eff}}(\boldsymbol{\kappa}) \\ \text{s.t.} \quad & \boldsymbol{\kappa} \leq \mathbf{1} \\ & \boldsymbol{\kappa} \geq \mathbf{0} \end{aligned} \tag{31}$$

where $\mathbf{1}$ and $\mathbf{0}$ denote 26×1 all-one and all-zero vectors, respectively. However, because of the inherent high dimensionality and nonlinearity of the problem, a solution was reached via four distinct steps. The approach for identifying suitable IM steering vectors was based on an initial dimensional reduction of the 26-dimensional problem, which could be solved through a meaningful approach in an acceptable runtime. It should be noted, however, that this dimensional reduction is likely to yield a local optimum rather than the global optimum of the OP. A detailed analysis for deriving the global optimum is beyond the scope of this paper. The initial two steps were undertaken with the objective of optimizing the IM steering coefficients, with a distinction made between those transmitted in I-phase (i.e., IM terms 1, 7, 8, 9, 10, 11, 12, 13, 14, 15, and 16) and those transmitted in Q-phase (i.e., IM terms 2, 3, 4, 5, 6, 17, 18, 19, 20, 21, 22, 23, 24, 25, and 26). In the initial stage of the process, a two-dimensional brute-force search is conducted, employing a method of iterative grid shrinking. The search grid is a uniformly spaced 21×21 grid comprising 441 test points within the domain $[0, 1] \times [0, 1]$. The brute-force search was implemented as a greedy search, whereby the optimal result was passed to a subsequent brute-force search that shrunk the search grid by a factor of 0.5. This process was repeated three times before proceeding to the subsequent step. In the second step, the best result was further optimized by using

TABLE 3

Power Distribution Results of 26-Dimensional Scalable Interplex Optimization for All Power Mode and HPA Combinations

HPA	Power Mode	$\frac{P_1^{(6)}}{P^{(6)}}$	$\frac{P_2^{(6)}}{P^{(6)}}$	$\frac{P_3^{(6)}}{P^{(6)}}$	$\frac{P_4^{(6)}}{P^{(6)}}$	$\frac{P_5^{(6)}}{P^{(6)}}$	$\frac{P_6^{(6)}}{P^{(6)}}$	$\frac{P_{\mathrm{IM,opt}}}{P^{(6)}}$	ν_{opt}	ζ_{opt} / dB
1	I	0.3753	0.1706	0.1706	0.0171	0.0171	0.1877	0.0617	22.08%	0.731
2	I	0.3810	0.1732	0.1732	0.0173	0.0173	0.1905	0.0475	17.01%	0.809
3	I	0.3867	0.1758	0.1758	0.0176	0.0176	0.1933	0.0334	11.94%	0.921
4	I	0.3998	0.1817	0.1817	0.0182	0.0182	0.1999	0.0006	00.20%	1.209
1	II	0.4048	0.1840	0.1840	0.0184	0.0184	0.1349	0.0555	22.81%	0.567
2	II	0.4085	0.1857	0.1857	0.0186	0.0186	0.1362	0.0469	19.28%	0.635
3	II	0.4156	0.1889	0.1889	0.0189	0.0189	0.1385	0.0304	12.48%	0.732
4	II	0.4285	0.1948	0.1948	0.0195	0.0195	0.1428	0.0001	00.04%	0.970

the Nelder–Mead simplex method (NMM). In the third step, a further distinction is made between high-frequency and low-frequency IM coefficients. The IM terms were designated as high-frequency terms if they contained the product of five signal terms (i.e., IM terms 1–6) or as low-frequency terms if they contained the product of three signal terms (i.e., IM terms 7–26).With the distinction of I-phase or Q-phase at the outset, a four-dimensional problem was formulated and solved using the NMM. In the final step, all IM terms were considered independently, thus necessitating a 26-dimensional optimization based on the optimization result of the four-dimensional problem. This procedure was performed for each HPA model and power mode combination.

The resulting power distributions, fractions of IM power spent compared with the standard interplex, and joint receiver efficiency gains for each power mode and HPA combination are reported in Table 3. In all combinations with HPA 1–3, neither the full use nor the full omission of IM terms is found to be optimal. Depending on the HPA model and power mode, the IM power ratio ν_{opt} for the scalable interplex ranges between 11.94% and 22.81%. The scalable interplex method exhibits the inherent capability to allocate the power distribution among the signal terms in a manner that is solely determined by the modulation angles θ_1, …, θ_N, irrespective of the chosen IM steering vector κ (Vergara & Antreich, 2013). Consequently, the power reduction of the IM component by scalable interplex, as observed in the studied cases, results in a redistribution of over 77.19% of the IM power to the useful signal components, in comparison to the standard interplex approach. The power share $P_{\mathrm{IM,opt}}/P^{(6)}$ of the optimized IM component reaches a maximum in cases where saturation-region HPA 1 is employed, as this HPA model features the lowest OBO, necessitating a greater IM component power allocation compared with the other HPA models with larger OBOs. When the idealized HPA model 4 is applied, the almost full omission of IM terms was found to be optimal, as the maximization of η_{eff} is implicitly constrained by the use of the HPA model and therefore its maximum output power. Indeed, using HPA 4 corresponds to neglecting an AM/AM deformation constraint.

To summarize, in the full IM case, the available transmit power remains unused, which can be exploited by the scalable interplex methodology. In the IM omission case, the signal components are transmitted with the maximum available power but are more severely affected by HPA distortions such that this configuration is sub-optimal. Intermediate levels of IM power use were found to be optimal. The optimal IM steering coefficient vector κ_{opt} depends on the HPA model and the interplex power mode.

4 | NUMERICAL RESULTS

This section presents simulation parameters and numerical results for the case study of the addition of a sixth signal component to the already transmitted Galileo E1 components.

4.1 | Simulation Parameters

The total path loss is set to –174 dB, which incorporates the transmitting antenna gain, implementation losses, atmospheric losses, free space loss, and receiving antenna gain. Based on the target average output power of 15.5 dBW for the HPA models, the reception power amounts to –158.5 dBW, which is a typical value of reception power in GNSSs according to Joseph (2010). The noise density was set to $N_0 = -204$ dBW/Hz, which corresponds to a receiver noise temperature at room temperature (Joseph, 2010). The modeled observation time window and correlator spacing were $T_0 = 20$ ms and $\Delta = 9.7752\ \text{ns} = T_{c,1}/40 = T_{c,2}/100 = T_{c,3}/100 = T_{c,4}/100 = T_{c,5}/100 = T_{c,6}/100$, respectively. Furthermore, the receiver was modeled ideally, by applying no quantization and correlating the filtered satellite contribution $s(t)$ with the replicas $\bar{x}_i(t)$, as indicated in Equation (7). The receiver front-end has a brick-wall characteristic:

$$H_{\mathrm{RX}}(f,B) = \mathcal{F}\{h_{\mathrm{RX}}(t,B)\} = \begin{cases} 1 & |f| < B/2 \\ 1/2 & |f| = B/2 \\ 0 & \text{else} \end{cases} \tag{32}$$

where B denotes the two-sided receiver bandwidth and $\mathcal{F}\{.\}$ denotes the Fourier transform. The TOA estimation error SD results are presented for varying front-end bandwidths B.

4.2 | Analysis of Civil Signal Power Recovery

In this first assessment, the scenario of adding one new signal component is compared with the status quo, where the Galileo signal can be generated via a five-channel interplex. Adding a new component would not only diminish the signal power of the legacy signals, owing to the fraction of power allocated to the new signal, but would also result in an over-proportional increase in power spent on IM terms. When transitioning from a five-channel interplex with eleven IM terms to a six-channel interplex with 26 IM terms, the multiplexing efficiency alone would decrease from 86.49% to a range of 72.07%–75.68% when the standard interplex is applied as the CEM method for the investigated power modes (see Table 1). The civil legacy signal power would be decreased in a range from 1.249 dB to 1.761 dB, depending on the chosen power mode when the standard interplex is applied with the assumption of a constant transmit power, as reported by the gain $\tilde{G}$ in the third column of Table 4.

Applying the scalable six-channel interplex instead would result in consistent improvements, as less power is spent on IM terms and, therefore, the power share among useful signal components increases. Compared with the current status quo, scalable interplex with six components would still lead to a decrease in signal power given by G_{opt}, as shown in the fourth column of Table 4. However, the decrease induced by adding the new component would be less severe and could

TABLE 4
Losses in E1B and E1C Signal Power When a New Component is Added Using the Standard Interplex or Scalable Interplex Compared with the Current Standard Interplex with $\alpha = 2$

HPA	Power Mode	$\tilde{G}$ / dB	G_{opt} / dB	$G_{\mathrm{opt}} - \tilde{G}$ / dB
1	I	−1.761	−0.615	1.146
2	I	−1.761	−0.550	1.211
3	I	−1.761	−0.486	1.275
4	I	−1.761	−0.341	1.420
1	II	−1.249	−0.287	0.962
2	II	−1.249	−0.248	1.002
3	II	−1.249	−0.173	1.076
4	II	−1.249	−0.040	1.210

improve the situation; moreover, this decrease may even enable the transmission of a new component on current payloads (if a certain loss of signal power is deemed to be acceptable and an HPA lifetime assessment is positive). For the realistic HPA scenarios (1–3), 1.002–1.275 dB of civil legacy signal power could be recovered when a scalable interplex is adopted rather than the standard interplex. The power recovery achieved by scalable interplex is greater for power modes in which a more even power distribution is chosen (i.e., power mode I with $\alpha = \beta = 2$), as the baseline multiplexing efficiency is worse than that of more uneven power distributions.

4.3 | Analysis of Ranging Performance

This subsection presents a discussion on whether adopting a scalable interplex instead of a standard interplex scheme directly yields an increase in ranging performance for each signal component. The ranging performance is evaluated by using the TOA estimation error SD for each HPA and power mode for varying receiver bandwidths B. Scalable interplex enhances the SNR portion in Equation (27), but employing QCEM instead of CEM will distort the shape of the CCF, as nonlinear effects introduced by the HPA affect the transmit signal. The results for the standard interplex will vary for each power mode, but remain the same for the considered HPA region of operation. The results of the scalable interplex vary for each power mode and HPA operation region. Figures 4 and 5 show the TOA estimation error SD with respect to the receiver bandwidths for all HPA operating regions and power modes I and II, respectively. Tables 5, 6, 7, and 8 report the relative performance changes in the TOA estimation error SD for five selected receiver bandwidths for the eight HPA and power mode combinations. The base value was the TOA estimation error SD of the standard interplex. A decrease in TOA estimation error SD corresponds to an improvement in ranging accuracy; conversely, an increase in TOA estimation error SD corresponds to a degradation in ranging performance.

Across all power modes, the results generally show that the TOA estimation error SD for BOC$_{\mathrm{cos}}$-R(15, 2.5) has a decreasing trend for higher power modes while the values for the other components show an inreasing trend due to the different power allocation. Interestingly, the scalable interplex operation states appear to favor the first and last component in comparison to the other two components. BOC$_{\mathrm{cos}}$-R(15, 2.5) experiences reductions in its TOA estimation error SD ranging from 9% to 18% compared with the standard interplex result. The BPSK-RC(1, 0.22) experiences a ranging performance increase in a range from 1% to 5%. However, the performance of BPSK-RC(1, 0.22) decreases for some HPA and power mode combinations.

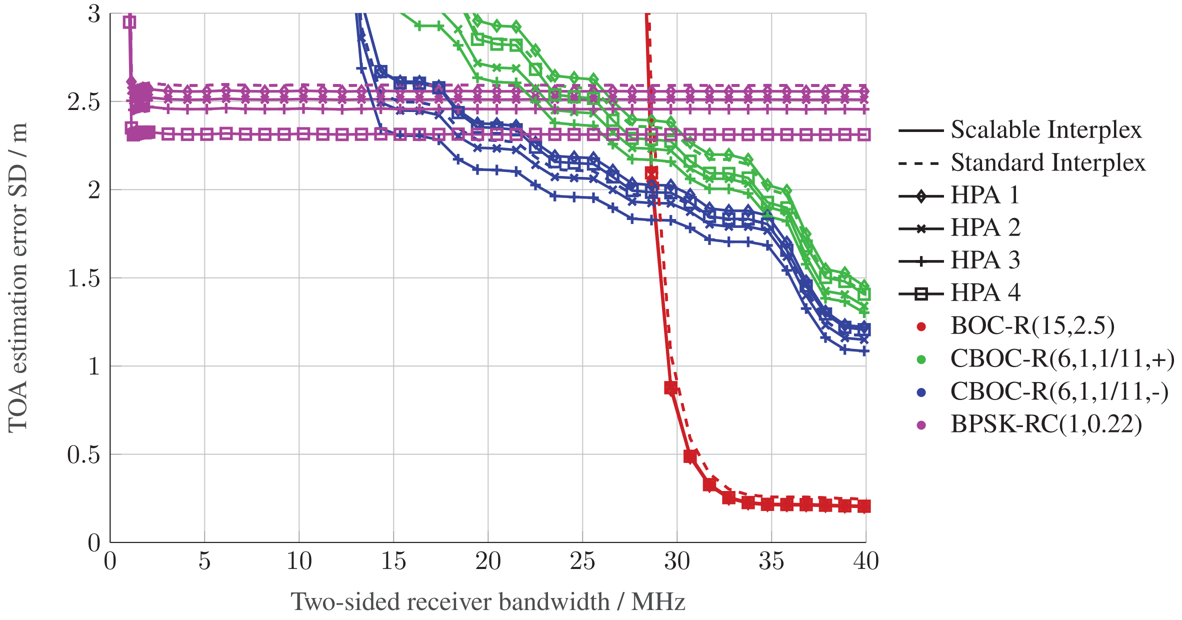

FIGURE 4 TOA estimation error SD for all HPA models and power mode I for varying receiver bandwidths

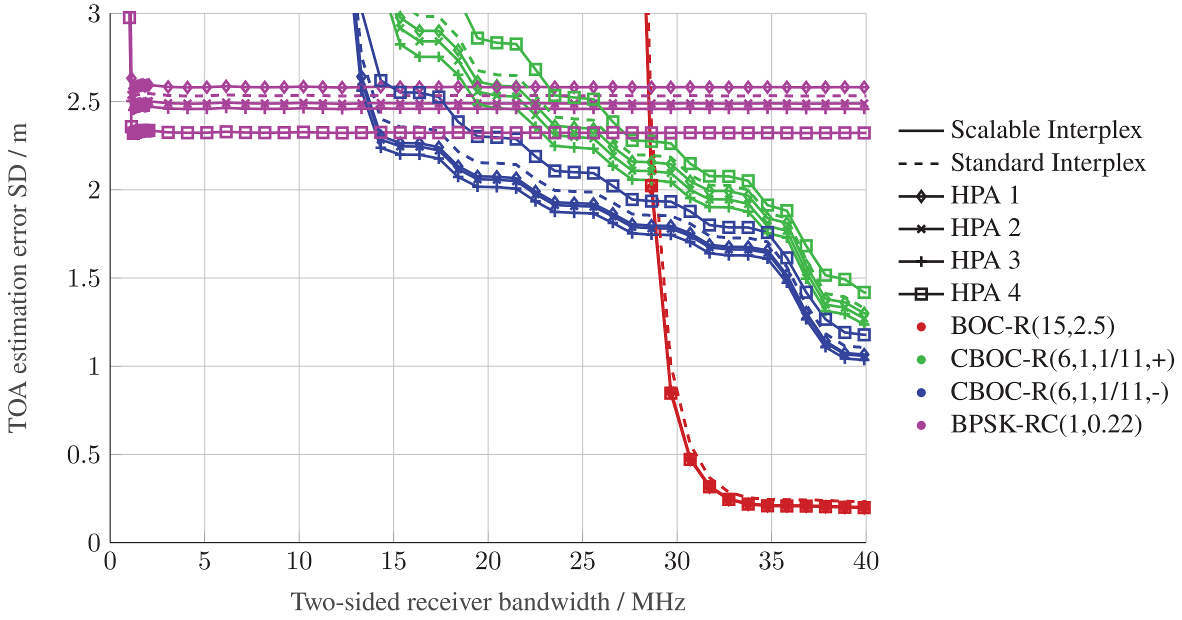

FIGURE 5 TOA estimation error SD for all HPA models and power mode II for varying receiver bandwidths

The results for power mode I shown in Figure 4 demonstrate that BPSK-RC(1, 0.22) would benefit in all HPA scenarios. However, CBOCs would deteriorate in ranging performance when using HPA 1 as well as HPA 4 for CBOC(6, 1, 1/11,–). Moreover, for any other HPA model, the scalable interplex found operating states that improved the ranging performance. In Figure 5, we can observe that, for power mode II, BPSK-RC(1, 0.22) would experience a decrease in ranging performance only in case of HPA 4. The CBOCs would also deteriorate in ranging performance for HPA 4. The application of any other HPA model results in improved ranging performance for all signals when scalable interplex is applied instead of the standard interplex.

5 | CONCLUSION

Higher-order scalable interplex represents a multiplexing method that enables the adaptation of a signal constellation to a specific realization of an HPA. This study examined the implications of incorporating a non-constant-envelope low-complexity signal component on the same carrier for the Galileo E1 signal, with regard to signal power losses and alterations in the TOA estimation error SD. The optimization of the joint receiver power efficiency consistently yields performance improvements in terms of recovered signal power, with less than 75% of the IM power required by the standard interplex. The determination of the IM steering coefficients is contingent upon the operational parameters of the HPA and the distribution of user signals in terms of power. It is also noteworthy that the identified scalable interplex solutions demonstrated an improved performance in the majority of cases. Thus, it may be advisable to consider a modified version of scalable interplex or an advanced QCEM scheme when adding future ranging signals.

Further research could assess ranging performance in terms of the Cramer–Rao and/or Ziv–Zakai lower bound, which would eliminate the dependence of the results on correlator spacing. Additionally, a comparative analysis of QCEM and CEM methods could be conducted. Furthermore, the objective function utilized in this study, which was employed to derive the scalable interplex IM steering vector, could be augmented or replaced with a ranging performance metric, thereby ensuring consistent ranging performance enhancements.

ACKNOWLEDGMENTS

This work has been carried out within the framework of the project NAV 4.0 within the German Aerospace Center (DLR). The work of Felix Antreich was supported by the Brazilian National Council for Scientific and Technological Development (CNPq) under grant 312394/2021-7 PQ-2. The authors thank the editors and reviewers for their time, effort, and insightful comments, which greatly contributed to the quality of this article.

CONFLICT OF INTEREST

The authors declare no potential conflict of interests.

REFERENCES

Allen, D. W., Arredondo, A., Barnes, D. R., Betz, J. W., Cerruti, A. P., Davidson, B., Kovach, K. L., & Utter, A. (2020). Effect of GPS III weighted voting on P(Y) receiver processing performance. *NAVIGATION*, *67*(4), 675–689. https://doi.org/10.1002/navi.394

Ávila Rodríguez, J. Á. (2008). *On generalized signal waveforms for satellite navigation* [Doctoral dissertation, Universitat der Bundeswehr Munchen]. https://athene-forschung.unibw.de/doc/86167/86167.pdf

Beck, F. C., Enneking, C., Thölert, S., & Antreich, F. (2022a). Comparison of constant and non-constant envelope signals for satellite navigation. *Proc. of the 2022 10th Workshop on Satellite Navigation Technology (NAVITEC)*, Noordwijk, Netherlands, 1–9. https://doi.org/10.1109/NAVITEC53682.2022.9847554

Beck, F. C., Enneking, C., Thölert, S., & Antreich, F. (2022b). Impact of omitting intermodulation products on ranging performance in satellite navigation. *Proc. of the 35th International Technical Meeting of the Satellite Division of the Institute of Navigation (ION GNSS+ 2022)*, Denver, CO, 1031–1045. https://doi.org/10.33012/2022.18315

Betz, J. W., & Kolodziejski, K. R. (2009). Generalized theory of code tracking with an early-late discriminator part I: Lower bound and coherent processing. *IEEE Transactions on Aerospace and Electronic Systems*, *45*(4), 1538–1556. https://doi.org/10.1109/TAES.2009.5310316

Butman, S., & Timor, U. (1972). Interplex - An efficient multichannel PSK/PM telemetry system. *IEEE Transactions on Communications*, *20*(3), 415–419. https://doi.org/10.1109/TCOM.1972.1091213

Dafesh, P. A., & Cahn, C. R. (2009). Phase-optimized constant-envelope transmission (POCET) modulation method for GNSS signals. *Proc. of the 22nd International Technical Meeting of the Satellite Division of the Institute of Navigation (ION GNSS 2009)*, Savannah, GA, 2860–2866. https://www.ion.org/publications/abstract.cfm?articleID=8701

Dafesh, P. A., & Cahn, C. R. (2011). Application of POCET method to combine GNSS signals at different carrier frequencies. *Proc. of the 2011 International Technical Meeting of the Institute of Navigation*, San Diego, CA, 1201–1206. https://www.ion.org/publications/abstract.cfm?articleID=9571

Enneking, C., Beck, F. C., Thölert, S., & Antreich, F. (2022). Transmit pulse shaping for 1-bit GNSS receivers. *2022 International Conference on Localization and GNSS (ICL-GNSS)*, 01–06. https://doi.org/10.1109/ICL-GNSS54081.2022.9797019

Joseph, A. (2010). Measuring GNSS signal strength. https://insidegnss.com/measuring-gnss-signal-strength/

Katz, A., Dorval, R., Gray, R., & Tenev, C. H. (2023). Versatile linearized miniature TWTAs for phased arrays in space. *Proc. of the 2023 IEEE Space Hardware and Radio Conference*, Las Vegas, NV. https://doi.org/10.1109/sharc56958.2023.10046268

Katz, A., Wood, J., & Chokola, D. (2016). The evolution of PA linearization: From classic feedforward and feedback through analog and digital predistortion. *IEEE Microwave Magazine*, *17*(2), 32–40. https://doi.org/10.1109/mmm.2015.2498079

Lestarquit, L., Artaud, G., & Issler, J.-L. (2008). AltBOC for dummies or everything you always wanted to know about AltBOC. *Proc. of the 21st International Technical Meeting of the Satellite Division of The Institute of Navigation (ION GNSS 2008)*, Savannah, GA, 961–970. https://www.ion.org/publications/abstract.cfm?articleID=8018

Ma, J., Yao, Z., & Lu, M. (2019). An efficiency optimal dual-frequency constant-envelope multiplexing technique for GNSS signals. *GPS Solutions*, *23*(3). https://doi.org/10.1007/s10291-019-0862-y

Meurer, M., & Antreich, F. (2017). Signals and modulation. In P. J. G. Teunissen & O. Montenbruck (Eds.), *Springer handbook of global navigation satellite systems,* 91–119. Springer International Publishing. https://doi.org/10.1007/978-3-319-42928-1_4

Nardin, A., Dovis, F., Perugia, S., Cristodaro, C., & Valle, V. (2023). Optimised design of next-generation multiplexing schemes for global navigation satellite systems. *IET Radar, Sonar & Navigation*, *17*(7), 1100–1104. https://doi.org/10.1049/rsn2.12403

Ortega, L., Poulliat, C., Boucheret, M. L., Aubault-Roudier, M., & Al-Bitar, H. (2020). New multiplexing method to add a new signal in the Galileo E1 band. *IET Radar, Sonar & Navigation*, *14*(11), 1735–1746. https://doi.org/10.1049/iet-rsn.2020.0197

Ortega Espluga, L., Poulliat, C., Boucheret, M.-L., Aubault, M., & Al Bitar-El Natour, H. (2020). *Technical note: Mathematical development of the interplexing 6 signals for the Galileo E1 band* (tech. rep.) (Version with last modification on February 2, 2024). Télécommunications Spatiales et Aéronautiques (TéSA). Toulouse, France. https://hal.science/hal-02944923

Proakis, J. G. (2001). *Digital communications*. McGraw-Hill. https://books.google.de/books?id=sbr8QwAACAAJ

Rapp, C. (1991). Effects of HPA-nonlinearity on a 4-DPSK/OFDM-signal for a digital sound broadcasting system. *Proc. of the Second European Conference on Satellite Communications (ECSC-2),* Liege, Belgium, 179–184. https://elib.dlr.de/33776/

Rebeyrol, E., Macabiau, C., Ries, L., Issler, J.-L., Bousquet, M., & Boucheret, M.-L. (2006). Interplex modulation for navigation systems at the L1 band. *Proc. of the 2006 National Technical Meeting of the Institute of Navigation*, Monterey, CA, 100–111. https://www.ion.org/publications/abstract.cfm?articleID=6514

Saleh, A. A. M. (1981). Frequency-independent and frequency-dependent nonlinear models of TWT amplifiers. *IEEE Transactions on Communications*, *29*(11), 1715–1720. https://doi.org/10.1109/tcom.1981.1094911

Spilker, J. J., & Orr, R. S. (1998). Code multiplexing via majority logic for GPS modernization. *Proc. of the 11th International Technical Meeting of the Satellite Division of the Institute of Navigation (ION GPS 1998)*, Nashville, TN, 265–273. https://www.ion.org/publications/abstract.cfm?articleID=2955

Thölert, S., Hauschild, A., Steigenberger, P., Langley, R. B., & Antreich, F. (2018). GPS IIR-M L1 transmit power redistribution: Analysis of GNSS receiver and high-gain antenna data. *NAVIGATION*, *65*(3), 423–430. https://doi.org/10.1002/navi.250

Vergara, M., & Antreich, F. (2013). Evolution of interplex scheme with variable signal constellation. *Proc. of the 2013 International Technical Meeting of the Institute of Navigation*, San Diego, CA, 651–770. https://www.ion.org/publications/abstract.cfm?articleID=10840

Vergara, M., Antreich, F., Enneking, C., Sgammini, M., & Seco-Granados, G. (2019). A model for assessing the impact of linear and nonlinear distortions on a GNSS receiver. *GPS Solutions*, *24*(1), 5. https://doi.org/10.1007/s10291-019-0917-0

Vergara, M., Antreich, F., Liva, G., & Matuz, B. (2013). Multi-service data dissemination for space-based augmentation systems. *Proc. of the 2013 IEEE Aerospace Conference*, Big Sky, MT, 1–7. https://doi.org/10.1109/AERO.2013.6496948

Wallner, S., García-Molina, J. A., Hahn, J., Risueno, G. L., Broi, G. d., Floch, J.-J., Soualle, F., Schmitt, T., Ouedraogo, M., Wörz, T., Vasquez, C., De Pasquale, G., & Paonni, M. (2021). Quasi-pilot signal design - Facilitating new signal processing concepts. *Proc. of the 34th International Technical Meeting of the Satellite Division of the Institute of Navigation (ION GNSS+ 2021)*, St. Louis, MO, 1859–1876. https://doi.org/10.33012/2021.17981

Wallner, S., García-Molina, J. A., Risueno, G. L., Hahn, J., Floch, J. J., Soualle, F., Schmitt, T., da Broi, G., Ouedraogo, M., Wörz, T., De Pasquale, G., Vasquez, C., & Paonni, M. (2020). Novel concepts on GNSS signal design serving emerging GNSS user categories: Quasi-pilot signal. *Proc. of the 2020 European Navigation Conference (ENC)*, Dresden, Germany, 1–22. https://doi.org/10.23919/ENC48637.2020.9317352

Won, J.-H., Fontanella, D., Paonni, M., Eissfeller, B., Emmanuele, A., Luise, M., Peña, A. J. G., Julien, O., Macabiau, C., Zanier, F., & Lopez-Risueno, G. (2011). Receiver architecture for multicarrier-based GNSS signals. *Proc. of the 5th GNSS Signal Workshop on GNSS Signal and Signal Processing (GSSP 2011)*, Toulouse, France. https://enac.hal.science/hal-01022488/

Yao, Z., Guo, F., Ma, J., & Lu, M. (2017). Orthogonality-based generalized multicarrier constant envelope multiplexing for DSSS signals. *IEEE Transactions on Aerospace and Electronic Systems*, *53*(4), 1685–1698. https://doi.org/10.1109/taes.2017.2671580

Yao, Z., & Lu, M. (2017). Signal multiplexing techniques for GNSS: The principle, progress, and challenges within a uniform framework. *IEEE Signal Processing Magazine*, *34*(5), 16–26. https://doi.org/10.1109/msp.2017.2713882

Yao, Z., & Lu, M. (2021). *Next-generation GNSS signal design: Theories, principles and technologies*. Springer Singapore. https://doi.org/10.1007/978-981-15-5799-6

Yao, Z., Ma, J., Zhang, J., & Lu, M. (2017). Multicarrier constant envelope composite signal - A solution to the next generation satellite navigation signals. *Proc. of the 30th International Technical Meeting of the Satellite Division of the Institute of Navigation (ION GNSS+ 2017)*, Portland, OR, 1520–1533. https://doi.org/10.33012/2017.15372

How to cite this article: Beck, F. C., Enneking, C., Thölert, S., & Antreich, F. (2025). Ranging performance evaluation for higher-order scalable interplex. *NAVIGATION, 72*(2). https://doi.org/10.33012/navi.702

A | REFORMULATIONS

For any $a \in \mathbb{R}$ and $\mathrm{b} \in \mathbb{R}$, the following angle addition theorems hold:

$$\sin(a \pm b) = \sin(a)\cos(b) \pm \cos(a)\sin(b) \tag{33a}$$

$$\cos(a \pm b) = \cos(a)\cos(b) \mp \sin(a)\sin(b) \tag{33b}$$

As an approximation, strictly bipolar signal components $x_n(t) \in \{-1, +1\}$ are assumed, which enables us to exploit the even symmetry of the cosine and the odd symmetry of the sine:

$$\cos(\theta_n x_n(t)) = \cos(\theta_n) \tag{34a}$$

$$\sin(\theta_n x_n(t)) = \sin(\theta_n)x_n(t) \tag{34b}$$

When assuming strictly bipolar signal components $x_n(t)$, we have the following:

$$\cos(\theta_n x_n(t)x_1(t)) = \cos(\theta_n) \tag{35a}$$

$$\sin(\theta_n x_n(t)x_1(t)) = \sin(\theta_n)x_n(t)x_1(t) \tag{35b}$$

for $n \in \{2, \ldots, N\}$. Additionally, one can use the following identities:

$$x_n^{2p+1}(t) = x_n(t) \tag{36a}$$

$$x_n^{2p}(t) = 1 \tag{36b}$$

for $p \in \mathbb{N}_0$ to simplify the equations further. Using the above identities, one can decompose Equation (10) to Equation (11) by setting the modulation angle of the first component $\theta_1 = \frac{\pi}{2}$.

B | TABLES

This section of the Appendix presents supplementary tables that illustrate the relative change in TOA estimation error SD for all four user replicas $\bar{x}_i \in i\{1,2,3,4\}$ when a six-channel scalable interplex is employed instead of the standard six-channel interplex. A negative value indicates a reduction in the code tracking jitter, which results in an improvement in ranging performance. Conversely, a positive value indicates an increase in the code tracking jitter, which results in a deterioration in ranging performance.

TABLE 5
Relative Change in Percent of TOA Estimation Error SD of the BOC$_{\text{cos}}$-R(15, 2.5) Component for Selected Receiver Bandwidths *B* When Using Scalable Interplex Compared with Standard Interplex

HPA	Power Mode	30.690 MHz	32.736 MHz	34.782 MHz	36.828 MHz	38.874 MHz	40.920 MHz
1	I	−18.36	−17.66	−18.02	−18.06	−18.06	−18.06
2	I	−16.94	−16.10	−16.50	−16.54	−16.56	−16.58
3	I	−16.10	−15.20	−15.65	−15.70	−15.71	−15.71
4	I	−17.12	−15.95	−16.53	−16.59	−16.62	−16.63
1	II	−15.30	−14.70	−15.00	−15.03	−15.03	−15.02
2	II	−13.94	−13.22	−13.56	−13.60	−13.61	−13.61
3	II	−13.78	−12.97	−13.35	−13.39	−13.40	−13.39
4	II	−15.18	−14.10	−14.59	−14.65	−14.67	−14.67

TABLE 6
Relative Change in Percent of TOA Estimation Error SD of the CBOC$_{\text{sin}}$-R(6, 1, 1/11, +) Component for Selected Receiver Bandwidths *B* When Using Scalable Interplex Compared with Standard Interplex

HPA	Power Mode	30.690 MHz	32.736 MHz	34.782 MHz	36.828 MHz	38.874 MHz	40.920 MHz
1	I	−5.21	−3.13	−3.34	3.45	2.08	1.24
2	I	−4.68	−4.31	−3.33	−5.90	−5.42	−5.07
3	I	−12.18	−9.92	−7.66	−8.92	−8.18	−7.69
4	I	−29.01	−21.23	−18.13	0.42	−2.08	−3.65
1	II	−1.86	−1.48	−0.47	−2.72	−2.03	−1.59
2	II	−3.52	−3.20	−2.37	−4.72	−4.27	−3.95
3	II	−7.16	−6.29	−4.57	−7.67	−6.75	−6.14
4	II	−22.77	−16.56	−15.09	9.06	5.05	2.52

TABLE 7

Relative Change in Percent of TOA Estimation Error SD of the CBOC$_{\sin}$-R(6, 1, 1/11,–) Component for Selected Receiver Bandwidths *B* When Using Scalable Interplex Compared with Standard Interplex

HPA	Power Mode	30.690 MHz	32.736 MHz	34.782 MHz	36.828 MHz	38.874 MHz	40.920 MHz
1	I	−3.93	−4.44	−3.13	4.66	3.54	2.74
2	I	−3.09	−3.25	−3.30	−1.94	−2.04	−2.15
3	I	−3.10	−2.94	−4.37	−7.62	−7.16	−6.87
4	I	−5.58	−7.07	−8.23	4.33	1.97	0.21
1	II	−0.54	−0.12	−0.43	−3.89	−3.33	−2.92
2	II	−2.05	−1.84	−2.29	−4.67	−4.12	−3.77
3	II	−1.78	−1.52	−2.82	−6.65	−6.08	−5.70
4	II	−3.91	−5.38	−5.91	8.30	5.48	3.48

TABLE 8

Relative Change in Percent of TOA Estimation Error SD of the BPSK-RC(1, 0.22) Component for Selected Receiver Bandwidths *B* When Using Scalable Interplex Compared with Standard Interplex

HPA	Power Mode	30.690 MHz	32.736 MHz	34.782 MHz	36.828 MHz	38.874 MHz	40.920 MHz
1	I	−0.16	−1.33	−1.33	−1.32	−1.32	−1.32
2	I	−3.38	−3.12	−3.12	−3.12	−3.12	−3.12
3	I	−6.76	−5.18	−5.19	−5.19	−5.20	−5.20
4	I	−14.90	−10.67	−10.70	−10.71	−10.71	−10.72
1	II	2.79	1.91	1.91	1.91	1.91	1.91
2	II	−1.63	−1.73	−1.73	−1.73	−1.72	−1.73
3	II	−4.09	−2.91	−2.92	−2.92	−2.92	−2.92
4	II	−11.91	−8.21	−8.24	−8.25	−8.26	−8.26